Research Article Vol. 33, No. 24 / 1 Dec 2025 / Optics Express 51434

Optics EXPRESS

Diffraction effects in highly defocused THz beams

FELIX GORKA,[1] ENRIQUE CASTRO-CAMUS,[1,2,*] DANIEL M. MITTLEMAN,[3] AND MARTIN KOCH[1]

[1]Department of Physics, Philipps-Universität Marburg, Renthof 5, 35032 Marburg, Germany
[2]Centro de Investigaciones en Optica A.C., Loma del Bosque 115, Lomas del Campestre, Leon, Guanajuato 37150, Mexico
[3]School of Engineering, Brown University, 184 Hope Street, Providence, Rhode Island 02912, USA
*enrique@cio.mx

Abstract: Terahertz communication links will require the use of directional beams to compensate for the higher losses compared to those faced in the few gigahertz region. The shorter wavelengths of terahertz waves also imply less diffraction from objects that may be present in many scenarios, such as books, bottles of water, or people. We present measurements of the frequency-dependent transmission losses for moderately divergent beams, with beam waists in the range of tens of centimeters, interacting with blockages. We compare our measurements with a quasi-optical treatment of these interactions based on the Fresnel diffraction theory. These results will inform the development of future generations of ultra-broadband communication technologies operating above 100 GHz.

1. Introduction

Commercial telecommunication systems such as cellular or WiFi operate almost exclusively in spectral bands below 10 gigahertz, with a corresponding wavelength in the few to few tens of centimetres range. At such long wavelengths, the presence of many typical obstacles in the line-of-sight path between the transmitter and receiver does not usually cause communication interruptions, particularly in indoor scenarios. One reason is because, although typical objects produce scattering losses, full shadowing of the signal is typically not an issue. Objects with size comparable to the wavelength generally do not produce sharp shadows; also, multiple scattering can extend coverage via non-line-of-sight paths.

This situation will change significantly with the use of higher frequencies in the sub-THz range [1–3], which is anticipated due to the large available bandwidth in unregulated bands above 100 GHz [4–6]. One of the challenges for the implementation of such high-frequency channels involves blockage effects. Unlike the lower frequency bands, THz communication links will require highly directional beam forming [7–11], given the high free-space path loss even for short-range links. This, in combination with the reduced scattering due to the shorter wavelengths, implies the value of considering such links in the context of directional optical signals [12]. It is therefore to be expected, that propagation of signals will need to be treated in such a way that scattering is properly accounted for. For instance, in an office room, people move and they carry files, books, and other objects around. A good number of these objects are large compared to the THz wavelengths, but contain features that are comparable or even smaller. Some early modeling of THz communication channels was performed using ray-tracing methods [13]. The use of beams with moderate divergence seems to be the most realistic solution for THz communications. Under that assumption, we will require a way to treat full frequency-dependent interaction of such beams with objects and people in order to get accurate channel models [14,15]. Diffraction phenomena for longer wavelengths in telecommunication channels have been discussed for larger objects such as buildings [16], walls or corners [14]. Some works have also investigated blockage

#575288 https://doi.org/10.1364/OE.575288
Journal © 2025 Received 5 Aug 2025; revised 26 Sep 2025; accepted 18 Oct 2025; published 26 Nov 2025

of indoor communication channels by objects and people in the sub-THz band [17] in the beam [18,19].

Here, we present an experimental study of the frequency-dependent blockage caused by a set of everyday objects, using a broadband defocused THz beam exhibiting moderately large divergence, which emulates a reasonable configuration for an indoor communication link at these frequencies. We compare our measured results to the predictions of Fresnel diffraction theory, showing that this formalism can be an appropriate theoretical tool for modeling blockage events in sub-THz communication channels.

2. Results

A terahertz time-domain spectrometer was adapted for a two-way path employing a large spherical mirror of 0.6 m effective diameter and 1.75 m radius of curvature. The setup is shown in Fig. 1(a) and a photograph of the mirror in Fig. 1(e). The emitter and detector were located adjacent to each other (±0.035 m apart), symmetrically displaced from the optical axis in the plane formed at the center of the sphere in such a way that the radiation generated at the emitter was refocused at the detector (Fig. 1(a)). The total propagation distance is therefore 3.5 m. Fig. 1(b) and (c) show the acquired time-domain signal, with no objects in the beam path, and the corresponding power spectrum. We emphasize that the spectrum is extremely broad, with the wavelength varying by more than one order of magnitude within the usable bandwidth of the measured radiation. The spatial profile of the beam was determined to be well approximated as a Gaussian, using a knife-edge measurement (see Methods section for details), as shown in Fig. 1(d). From this result we calculate a full-power 3dB angular beam width of 10.7 °.

After initial characterization of the system performance which serve to define the reference field E_{ref}, we then acquire similar measurements with a variety of objects in the beam path E_{obj}, at locations A, B, and C illustrated in Fig. 1(a). The THz beam diameter increases from location A to C and represents blockage scenarios for different distances to the transmitter. As examples, we select several typical objects, which could produce blockage of a THz communication channel in an office scenario: a book, a water bottle and a metallic tube. We define the (frequency-dependent) transmission as the ratio of the measured signals with and without objects in the beam, as

$$T = \left|\frac{E_{\text{obj}}(\nu)}{E_{\text{ref}}(\nu)}\right|^2, \tag{1}$$

where E_{obj} and E_{ref} are the Fourier transform of the electric field waveform obtained in the presence and absence of objects respectively as a function of frequency ν. We can anticipate a non-trivial frequency dependence because the ratio of the wavelength to the feature sizes in our objects varies significantly within the bandwidth of the radiation used here. The measurement results for the three objects are shown in Fig. 2(a)-(c). We observe that, in all cases, the measurements show an initial decrease in transmission reaching a minimum in the region between 200 and 500 GHz, followed by an increase that stabilizes for frequencies above about 750 GHz. The book shows the lowest transmission, followed by the bottle and subsequently the tube. This trend is consistent with the trend in cross-sectional area of the objects. The three curves shown in each panel represent the three locations A (paler color), B and C (darker color) as indicated in Fig. 1(a). We observe an decrease in transmission with increasing distance from the curved mirror. This is also expected, since there is more significant obstruction of the beam when the beam is smallest, which is the case for location A farthest from the mirror, as illustrated in Fig. 1(a).

The plots in Fig. 2(d-f) show the results of diffraction calculations using the Fresnel integral formula, which can be regarded as *a priori* predictions of the measurement results [20]. Details of the calculation method are described in the Methods section. These numerical results show a qualitatively consistent behaviour with the experimental measurements, including both the trends

Optics EXPRESS

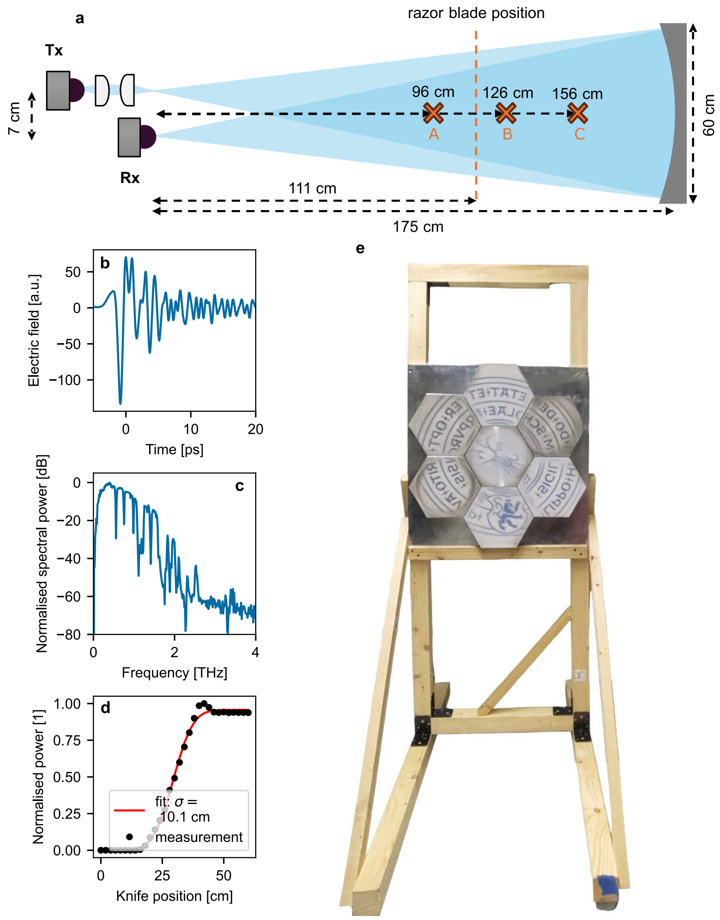

Fig. 1. (a) Optical setup for the THz TDS measurements and positions of the object within the THz beam. Optical components are not drawn to scale. The axial positions are measured from the intermediate focus. (b) THz-TDS waveform obtained after passing through the setup without object. (c) Power spectrum of the transmitted pulse. (d) Razor-blade measurement and error function fit to determine the beam diameter. (e) Photograph of the segmented mirror while it produces an optical image mounted on a home-built wooden kinematic mount.

with object size and object location. They also reproduce the small but repeatable minimum in the measured signals at frequencies below 500 GHz. This minimum is the result of the scattering power distribution at the focal plane where the detector is.

In order to illustrate the reason for this spectral dip with an example, in Fig. 3(b) we have reproduced the curve for the transmission around the bottle at position A. Three markers are placed at the frequencies where the spectral dip starts (150 GHz), reaches its minimum (300 GHz), and ends (675 GHz). In Fig. 3(c), we show the power distribution as a function of the horizontal position (x) and the frequency (for y=0) in the vicinity of the focal point. White lines are provided as a reference of the limits of the aperture of our detector, and three markers are placed as a visual reference of the frequencies consistently with panel a. In Fig. 3(d), the reference power distribution, in the absence of the bottle, also at the focus is shown for comparison. It is easy to see in Fig. 3(b) that diffraction fringes produced by the bottle merge towards the focus as the frequency increases. For frequencies below 150 GHz the object and reference power distributions

Optics EXPRESS

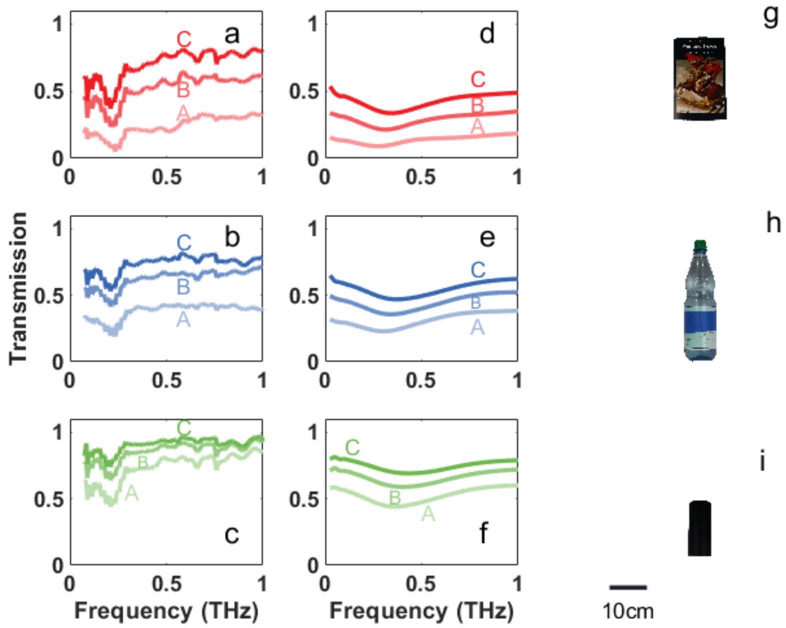

Fig. 2. Experimental power-transmission measurements as function of the frequency (a-c) as well as the calculation of the transmission based on the Fresnel integral calculation (d-f) for the objects shown (g-i). The pale coloured curves correspond to position A, followed by B and the dark colour curves correspond to position C as depicted in Fig. 1.

seem to have a similar behavior, namely, the focal spot decreases with frequency, which implies an increase of the total power that falls within the aperture of the detector. Yet, at around 150 GHz there is a qualitative difference between the two power distributions; while the size of the reference beam continues to decrease (implying an increase of the collected signal), the scattered signal begins to incorporate a null (diffraction minimum) into the collection aperture. This effectively decreases T in accordance with Eq. (1). For frequencies between 300 GHz and 675 GHz, a diffraction maximum merges into the aperture, thus increasing T. At higher frequencies, weaker diffraction effects produce only small fluctuations in the signal.

There are of course discrepancies between the experimental and theoretical curves, which may result from small unavoidable uncertainties in the precise positioning and orientation of the objects relative to the central optic axis of the beam or imperfections in the optical alignment. Nevertheless, the qualitative agreement is satisfactory, suggesting that our computational approach describes these scenarios with reasonable accuracy. Yet, we must point out that the quantitative discrepancies between the model and the measurements can be caused by two factors. Firstly, the emission pattern of the photoconductive antennas is not perfectly Gaussian (Discussed with Lars Liebermeister, HHI/Fraunhofer, Berlin, Germany). Secondly, the interaction of the wave with the aperture and hyperhemispherical mirror of the detector is not accounted for accurately in our model (Discussed with Nurial Lombardt, TU Delft, Delft, Netherlands). In order to have a more quantitative comparison of the measurements and experiments, we compared the transmission values at 0.1 THz, 0.3 THz and 1 THz for all the curves in Fig. 2(a)-(f). This correlation plot is shown in Fig. 3(a). We observe that the theoretically calculated transmissions are consistently lower than the measurements, but they do show a relatively strong correlation, with a correlation coefficient of 0.874.

In addition to inanimate objects, we also performed similar measurements using people, aiming to recreate the evolution of a communication channel in a dynamic scenario. In Fig. 4(a)-(c) show

Optics EXPRESS

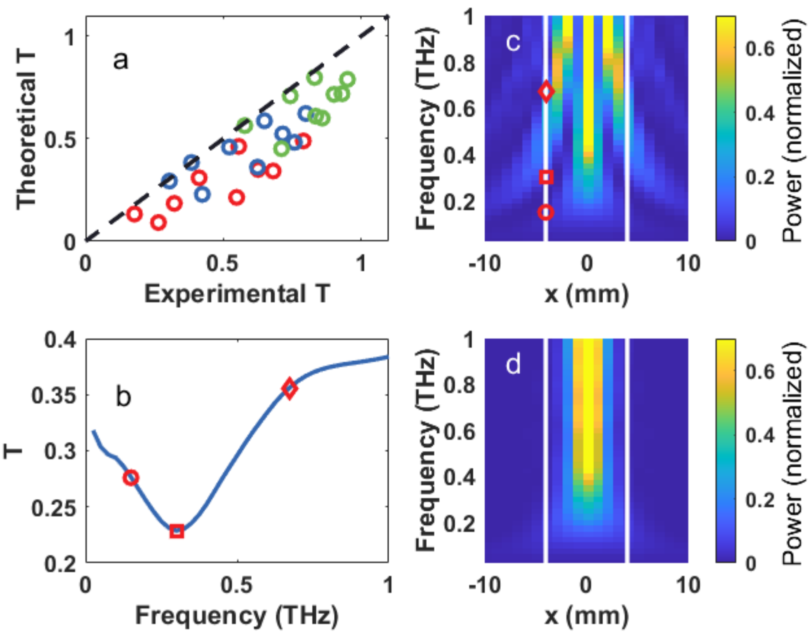

Fig. 3. (a) Correlation of the theoretical and experimental transmissions as for the data presented in Fig. 2(a)-f at frequencies 0.1 GHz, 0.2 GHz and 1 THz. The colors of the dots are consistent for each object. The theoretical calculations and experimental measurements have a correlation coefficient of 0.874. (b) Theoretically predicted transmission spectrum for a bottle in position A. Three markers (circle, square and diamond) are placed at 150 GHz, 300 GHz and 675 GHz which correspond to the points in which the transmission dip of the spectrum starts, reaches its minimum and ends respectively. (c) Colormap representing the power distribution predicted theoretically across the focal plane where the detector is placed when a water bottle is present at position A. Two white lines indicate the aperture of our detector. Markers (circle, square and diamond) are placed at 150 GHz, 300 GHz and 675 GHz respectively consistently with panel (b). (d) Colormap representing the power distribution predicted theoretically across the focal plane where the detector is placed in the absence of object. Two white lines indicate the aperture of our detector.

the analogous results when a hand is inserted into the beam path (stationary) at each of the same three approximate locations referenced above. Here, due to the difficulty in precisely locating the obstruction relative to the optic axis, the disagreement between measurement and prediction is somewhat larger. Indeed, the strongly increasing trend of transmission with frequency is notably different from the results obtained with static objects, and is not reproduced in the numerical simulations. This may be a result of diffraction not only by the hand and arm, but also by the rest of the body of the person which is not in the central part of the beam, but will still interact with it.

Finally, Fig. 4(d)-(f) show a set of measurements and calculations for a person at different positions across the beam. Here, the results are displayed as false color maps where the horizontal axis shows subsequent frames of a motion series representing sequential moments in time. The measurements (Fig. 4(d) and Visualization 1) were obtained with the subject at a distance of ∼1.1 m from emitter/detector position. The corresponding simulations are shown in Fig. 4(e). The frame number is related to the motion of the person across the beam (increasing as the person moves from right to left). For the first (before the person has entered the beam) and last (after completely passing) frames, the transmission is very high, but the frames in the middle show negligible transmission since the person is almost entirely blocking the signal. The experimental

Optics EXPRESS

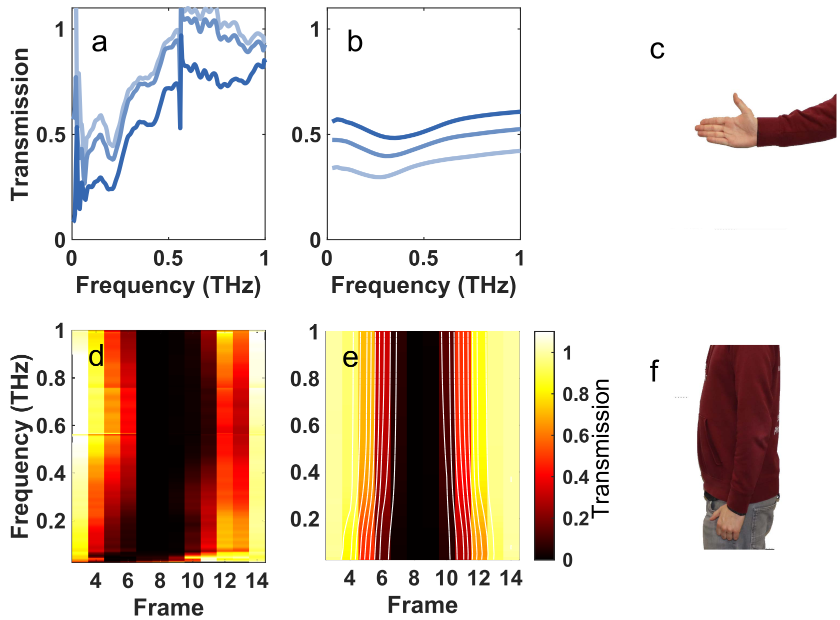

Fig. 4. Experimental power-transmission measurements as function of the frequency (a) as well as the calculation of the transmission based on the Fresnel integral calculation (b) for a human hand shown (c). The colormap (d) represents the transmitted power measured for different moments of a person walking across the beam. The colormap (e) shows the analogous theoretical calculations based on a series of photographs like the one shown in (f), isocurves where added in on this map as a guide-to-the-eye.

and predicted results show consistent behavior with each other. Due to the relatively slow data acquisition time for our TDS apparatus, these measurements are relatively coarse, with significant changes in the signal between adjacent measurements. That being said, we highlight that the calculations in Fig. 4(e) show that the width of the dark band decreases as the frequency increases. This frequency-dependent effect is not visible in our broadband measurements due to the limited number of frames acquired during the motion of the subject. Yet, we note that related measurements have recently reported similar results, [21] noting a consistent difference between the duration of blockage at 60 GHz versus 300 GHz. This difference is caused by the more delocalized interaction of longer wavelengths $\lambda = 5$ mm (at 60 GHz) compared to $\lambda = 1$ mm (at 300 GHz).

3. Discussion

We presented a series of measurements and diffraction calculations of objects and a person interacting with a broad-band terahertz beam. This experiment demonstrates that the degree of "blockage" is highly frequency dependent. The Fresnel diffraction formula provides a solid theoretical tool to estimate the transmittance resulting from the diffraction around objects and people. With this formula it is possible to also calculate the diffraction patterns. This will be an invaluable tool for modelling the propagation of terahertz communication channels in realistic scenes where objects with dimensions and features larger and smaller than the wavelength can be taken into account properly. This approach also provides an alternative to ray tracing, which is a rather coarse approximation, that might be inappropriate for the modelling of telecommunication channels in scenes with complex blockage geometries.

Optics EXPRESS

4. Methods

4.1. Mirror fabrication

A concave spherical mirror with a radius of curvature $r = 1.75$ m consisting of seven hexagonal segments with 17.3 cm edge length was manufactured by CNC milling of solid aluminium. The individual segments were polished to near optical quality against a stamp cast out of optical grade pitch (32° CZ hardness, Pieplow&Brandt GmbH) to match the curvature of the mirror. A slurry of 2μ m average diameter 30 g/L Al_2O_3 microspheres (ALUPOX 2.0, Pieplow&Brandt GmbH) in water was used as the polishing medium. Pitch polishing was continued until a clear optical image was formed by the mirror segment. Finally, the individual elements were mounted to form a segmented mirror of 60 cm diameter (longest axis).

4.2. THz time domain spectroscopy

The optical setup for the THz measurements is shown in fig:setup. Characterisation of the frequency-dependent transmission was performed by THz time-domain spectroscopy using a fibre-coupled TDS [22] system described elsewhere [23]. All measurements were performed by averaging 100 scans, except for measurements with a person (or part thereof) in the beam, which were done at 10 averages as the subject could not remain in position for longer. The THz beam emitted by the transmitter antenna was collected and brought to an intermediate focus by two plano-convex polyethylene lenses ($f = 6$ cm, d = 5 cm). The divergent THz beam was refocused on the receiver antenna by the large segmented mirror ($r = 1.75$ m, d = 60 cm) with a horizontal offset of 7 cm. Pre-alignment of the THz beam path was facilitated by producing an optical point source with another, visible laser at an iris aperture placed on the intermediate focus. For all THz measurements, the aperture remained fully opened to 25 mm. As the delay through the setup is much larger than the travel of the THz spectrometer's delay line, the THz pulse is detected by the $N + 1$ pulse from the fs-laser. Due to the size of the optical setup, all measurements were performed in air. The samples were supported by a block of expanded polystyrene, which was kept in the same position for the corresponding reference measurement. The beam diameter of the divergent THz beam was characterised through the razor blade method by retracting a metal sheet larger than the mirror aperture from the beam. The frequency dependent blockage was measured for three different axial positions (A, B, C) in order to present the samples to different beam diameters ($1\sigma = 5.5$ cm, 7.2 cm, 8.9 cm). The axial positions detailed in fig:setup are measured from the intermediate focus.

4.3. Data analysis

THz spectra were obtained from the Fourier transform of the detected waveform using an error-function filter to remove the reflections in the waveform. The transmission from the emitter to the detector is defined as in Eq. (1). The measurements were performed under normal atmosphere, therefore a series of spectral lines related to the water vapour presence appear in our spectra [24–26]. These lines have no relationship to the interaction of the object with the THz radiation and will not be discussed further.

4.4. Diffraction theory

The experiment was modelled by using the Fresnel integral formula, which allows us to calculate the evolution of an electric field known at a plane as it propagates to another plane further along. The Fresnel integral, based on the Huygens' principle, states that the electric field propagating from a plane, which we call the object plane, where the electric field is known, to another plane, which we call the screen plane, separated by a distance z is given by

$$E(x,y,z) = \int_{-\infty}^{+\infty}\int_{-\infty}^{+\infty} E(x',y',0)\exp\left(\frac{ik}{2z}[(x-x')^2+(y-y')^2]\right)dx'dy', \tag{2}$$

where (x,y) and (x',y') are the coordinates at the screen and object planes respectively. This integral requires rather large computational capacity to be solved numerically, yet, the integral can be seen as a 2-dimensional convolution of the electric field at the object plane $E(x',y',0)$ and the function $\exp(\frac{ik}{2z}[x^2+y^2])$, thus, by using the convolution theorem, the solution can be written as

$$E(x,y,z) = \mathcal{F}^{-1}\left[\mathcal{F}[E(x',y',0)]\times\mathcal{F}\left[\exp\left(\frac{ik}{2z}[(x')^2+(y')^2]\right)\right]\right], \tag{3}$$

where $\mathcal{F}$ and $\mathcal{F}^{-1}$ represent the 2-dimensional Fourier and inverse Fourier transforms respectively. Therefore, the numerical solution of the integral only involves the calculation of two fast Fourier transforms, which is computationally less expensive.

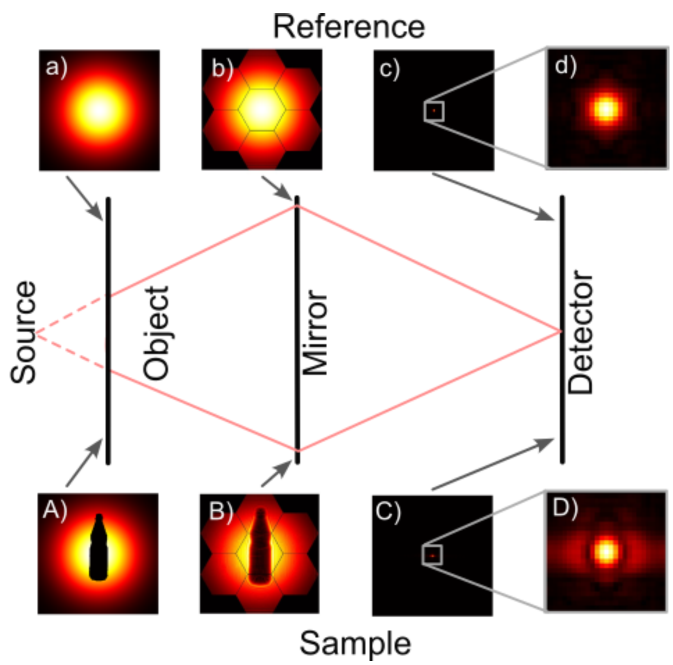

Fig. 5. Schematic representation of the theoretical propagation calculation performed using the Fresnel integral. The top panels (a-d) show the electric field distribution at different positions along the optical axis, namely the object, mirror and detector planes in the absence of of object. Panels (A-D) show the field distributions in the presence of an object (in this case a water bottle). The color-scales of the different panels are not consistent with each other, since this images are only for illustration purposes. The panels shown are the result of a simulation at 300 GHz. The quantitative comparison is shown in the results section.

In order to model the propagation of the radiation from the emitter to the detector, we took photographs (shown in Fig. 2(g-f), Fig. 4(c) and in the supplementary material) of the objects on a 0.6 m×0.6 m white background, these photographs were subsequently processed in order to generate a binary mask where object pixels were set to 0 and non-object pixels were set to 1. The image was then carefully scaled to match a 0.6 m×0.6 m area where each pixel represents a 100 μm×100 μm area. An initial electric field at the appropriate distance (A, B or C as shown in

Optics EXPRESS

Fig. 1(a)) was calculated with a Gaussian beam profile with a beam-waist consistent with the results of the razor blade measurement described earlier. Then, the amplitude of this beam is multiplied by the object-shaped mask as shown in Fig. 5(a). The divergence is adjusted by setting the phase of the wave at the object plane to

$$\phi(x, y, 0) = \frac{k}{2z_0}(x^2 + y^2), \tag{4}$$

where z_0 is the distance between the emitter and the object and $k = 2\pi/\lambda$, with λ being the wavelength. The electric field is then propagated to the mirror position by using Eq. (3), as shown in Fig. 5(b). In order to model the interaction of the terahertz radiation with the mirror, a filter composed of 7-hexagonal areas of 198 mm width with 2 mm separation between them is applied and the phase is once again multiplied by the function from Eq. (4) replacing z_0 by $-d/2$ where $d = 1.75$ m is the distance between the mirror and the detector. Then the field is propagated again using Eq. (3) in order to simulate the refocusing of the radiation onto the detector as depicted in Fig. 5(c,d). The resulting electric field is squared and integrated over an aperture of diameter 8 mm in order to calculate the expected power detected at the receiver in our experimental setup. The same treatment is done to the original Gaussian beam, but without applying the object mask in order to calculate the reference power that goes from the emitter to the receiver in the absence of object as depicted in Fig. 5(a)-(d). The ratio of the object and reference powers is then used to predict the transmittance that we obtain experimentally from Eq. (1).

Funding. Deutsche Forschungsgemeinschaft (FOR 2863); Alexander von Humboldt-Stiftung.

Disclosures. The authors declare no conflicts of interest.

Author contributions statement. E.C.C. and D.M.M. jointly conceived the study; F.G. conducted the experiment(s); E.C.C. performed the modeling; M.K. supervised the work; F.G. and E.C.C. wrote the manuscript with support from D.M.M. All authors reviewed the manuscript.

Data availability. Data underlying the results presented in this paper are available at [27].

References

1. R. Piesiewicz, M. Jacob, M. Koch, *et al.*, "Performance analysis of future multigigabit wireless communication systems at thz frequencies with highly directive antennas in realistic indoor environments," IEEE J. Sel. Top. Quantum Electron. **14**(2), 421–430 (2008).
2. T. Nagatsuma, G. Ducournau, and C. C. Renaud, "Advances in terahertz communications accelerated by photonics," Nat. Photonics **10**(6), 371–379 (2016).
3. M. Koch, "Terahertz communications: A 2020 vision," in *Terahertz frequency detection and identification of materials and objects*, (Springer, 2007), pp. 325–338.
4. T. Kürner, D. M. Mittleman, and T. Nagatsuma, "THz communications: Paving the way towards wireless tbps," *Springer Series in Optical Sciences* 234, (2016).
5. T. Kürner and S. Priebe, "Towards THz communications-status in research, standardization and regulation," J. Infrared, Millimeter, Terahertz Waves **35**(1), 53–62 (2014).
6. V. Petrov, T. Kürner, and I. Hosako, "Ieee 802.15. 3d: First standardization efforts for sub-terahertz band communications toward 6g," IEEE Commun. Mag. **58**(11), 28–33 (2020).
7. R. Piesiewicz, T. Kleine-Ostmann, N. Krumbholz, *et al.*, "Short-range ultra-broadband terahertz communications: concepts and perspectives," IEEE Antennas Propag. Mag. **49**(6), 24–39 (2007).
8. H.-J. Song and T. Nagatsuma, "Present and future of terahertz communications," IEEE Trans. Terahertz Sci. Technol. **1**(1), 256–263 (2011).
9. J. M. Jornet, E. W. Knightly, and D. M. Mittleman, "Wireless communications sensing and security above 100 GHz," Nat. Commun. **14**(1), 841 (2023).
10. O. El Ayach, S. Rajagopal, S. Abu-Surra, *et al.*, "Spatially sparse precoding in millimeter wave MIMO systems," IEEE Trans. Wireless Commun. **13**(3), 1499–1513 (2014).
11. F. Sohrabi and W. Yu, "Hybrid analog and digital beamforming for mmWave OFDM large-scale antenna arrays," IEEE J. Select. Areas Commun. **35**(7), 1432–1443 (2017).
12. W. Miller, "Proceedings of the symposium on quasi-optics, vol. 14," Proc. IEEE **53**(7), 766–767 (1965).
13. R. Piesiewicz, J. Jemai, M. Koch, *et al.*, "THz channel characterization for future wireless gigabit indoor communication systems," in *Terahertz and Gigahertz Electronics and Photonics IV*, vol. 5727, (SPIE, 2005), pp. 166–176.
14. M. Jacob, S. Priebe, R. Dickhoff, *et al.*, "Diffraction in mm and sub-mm wave indoor propagation channels," IEEE Trans. Microwave Theory Tech. **60**(3), 833–844 (2012).

Optics EXPRESS

15. M. A. Salhi, T. Kleine-Ostmann, and T. Schrader, "Propagation channel measurements in the mm- and sub-mm wave range for different indoor communication scenarios," J. Infrared, Millimeter, Terahertz Waves **42**(4), 357–370 (2021).
16. K.-W. Kim, M.-D. Kim, J. Lee, *et al.*, "Millimeter-wave diffraction-loss model based on over-rooftop propagation measurements," ETRI Journal **42**(6), 827–836 (2020).
17. B. De Beelde, E. Tanghe, C. Desset, *et al.*, "Office room channel modeling and object attenuation at sub-THz frequencies," Electronics (Basel, Switz.) **10**(14), 1725 (2021).
18. A. Shurakov, D. Moltchanov, A. Prikhodko, *et al.*, "Empirical blockage characterization and detection in indoor sub-THz communications," Computer Communications **201**, 48–58 (2023).
19. A. Shafie, N. Yang, S. Durrani, *et al.*, "Coverage Analysis for 3D Terahertz Communication Systems," IEEE J. Select. Areas Commun. **39**(6), 1817–1832 (2021).
20. D. G. Voelz, "Computational fourier optics: a matlab tutorial," SPIE Tutorial Texts in Optical Engineering **TT89**, 63–111 (2011).
21. T. Doeker, M. Eggers, C. E. Reinhardt, *et al.*, "Human motion sensing through blockage and reflection measurements at 60 GHz and 300 GHz," IEEE Access **13**, 97997–98005 (2025).
22. M. Koch, D. M. Mittleman, J. Ornik, *et al.*, "Terahertz time-domain spectroscopy," Nat. Rev. Methods Primers **3**(1), 48 (2023).
23. N. Vieweg, F. Rettich, A. Deninger, *et al.*, "Terahertz-time domain spectrometer with 90 dB peak dynamic range," J. Infrared, Millimeter, Terahertz Waves **35**(10), 823–832 (2014).
24. M. Van Exter, C. Fattinger, and D. Grischkowsky, "Terahertz time-domain spectroscopy of water vapor," Opt. Lett. **14**(20), 1128–1130 (1989).
25. J.-G. Kwon, M.-W. Park, and T.-I. Jeon, "Determination of the water vapor continuum absorption by THz pulse transmission using long-range multipass cell," J. Quant. Spectrosc. Radiat. Transfer **272**, 107811 (2021).
26. F. Taleb, M. Alfaro-Gomez, M. D. Al-Dabbagh, *et al.*, "Propagation of THz radiation in air over a broad range of atmospheric temperature and humidity conditions," Sci. Rep. **13**(1), 20782 (2023).
27. F. Gorka, E. Castro-Camus, D. M. Mittleman, *et al.*, "Diffraction effects in highly defocused thz beams - dataset," figshare (2025), https://doi.org/10.6084/m9.figshare.30217555.v1.